

An Engineering Solution for solving Mesh Size Effects in the Simulation of Delamination with Cohesive Zone Models

A. Turon^a, C.G. Dávila^b, P.P. Camanho^c, J. Costa^a

^a*AMADE, Polytechnic School, University of Girona, Campus Montilivi s/n, 17071 Girona, Spain*

^b*NASA Langley Research Center, Hampton, Virginia, U.S.A.*

^c*DEMEGI, Faculdade de Engenharia, Universidade do Porto, Rua Dr. Roberto Frias, 4200-465, Porto, Portugal*

Abstract

This paper presents a methodology to determine the parameters to be used in the constitutive equations of Cohesive Zone Models employed in the simulation of delamination in composite materials by means of decohesion finite elements. A closed-form expression is developed to define the stiffness of the cohesive layer. A novel procedure that allows the use of coarser meshes of decohesion elements in large-scale computations is also proposed. The procedure ensures that the energy dissipated by the fracture process is computed correctly. It is shown that coarse-meshed models defined using the approach proposed here yield the same results as the models with finer meshes normally used for the simulation of fracture processes.

Key words: Delamination, Fracture, Decohesion elements

1 Introduction

Delamination, or interfacial cracking between composite layers, is one of the most common types of damage in laminated fibre-reinforced composites due to their relatively weak interlaminar strengths. Delamination may arise under various circumstances, such as low velocity impacts, or bearing loads in structural joints. The delamination failure mode is particularly important for the structural integrity of composite structures because it is difficult to detect during inspection.

The simulation of delamination using the finite element method (FEM) is normally performed by means of the Virtual Crack Closure Technique (VCCT) [1], or using decohesion finite elements [2]-[10].

The VCCT is based on the assumption that the energy released during delamination propagation equals the work required to close the crack back to its original position. Based on this assumption, the components of the energy release rate are computed from the nodal forces and nodal relative displacements [1]. Delamination growth is predicted when a combination of the components of the energy release rate is equal to a critical value.

There are some difficulties when using the VCCT in the simulation of progressive delamination. The calculation of fracture parameters requires nodal variables and topological information from the nodes ahead and behind the crack front. Such calculations are tedious to perform and may require remeshing for crack propagation.

The use of decohesion finite elements can overcome some of the above difficul-

ties. Decohesion finite elements can predict both the onset and the non-self-similar propagation of delamination. However, the simulation of progressive delamination using decohesion elements poses numerical difficulties related with the proper definition of the stiffness of the cohesive layer, the requirement of extremely refined meshes, and the convergence difficulties associated with problems involving softening constitutive models.

This work addresses the proper definition of interface stiffness. A closed-form expression for the interface stiffness is developed, replacing the empirical definitions of the stiffness of the cohesive layer that are normally used. In addition, a solution that allows the use of coarse meshes in the simulation of delamination is proposed.

The kinematics and constitutive model of a previously proposed decohesion element [11]-[12], formulated for three-dimensional (3D) elements, is adapted to be used with two-dimensional (2D) finite element models. Finally, several simulations of specimens with and without initial cracks were performed, in order to demonstrate that the methodology proposed can accurately predict both crack initiation and propagation using coarse meshes.

2 Selection of Cohesive Zone Model parameters

2.1 Cohesive Zone Model approach

Decohesion finite elements are used to model material discontinuities. Consider a domain Ω containing a material discontinuity, Γ_d , which divides the domain Ω into two parts, Ω_+ and Ω_- , as shown in Figure 1.

[Figure 1 about here]

Prescribed tractions, t_i , are imposed on the boundary Γ_F , whereas prescribed displacements are imposed on the boundary Γ_u . The stress field inside the domain, σ_{ij} , is related to the external loading and to the closing tractions τ_j^+, τ_j^- in the material discontinuity through the equilibrium equations:

$$\sigma_{ij,j} = 0 \text{ in } \Omega \quad (1)$$

$$\sigma_{ij}n_j = t_i \text{ on } \Gamma_F \quad (2)$$

$$\sigma_{ij}n_j^+ = \tau_i^+ = -\tau_i^- = \sigma_{ij}n_j^- \text{ on } \Gamma_d \quad (3)$$

The formulation of the decohesion finite elements is based in the Cohesive Zone Model (CZM) approach. The CZM approach [13]–[15] is one of the most commonly used tools to investigate interfacial fracture. The CZM approach assumes that a cohesive damage zone, or softening plasticity, develops near the crack tip. The CZM links the microstructural failure mechanism to the continuum fields governing bulk deformations. Thus, a CZM is characterized by the properties of the bulk material, the crack initiation condition, and the crack evolution function.

Cohesive damage zone models relate traction, τ , to displacement jumps, Δ , at an interface where a crack may occur. Damage initiation is related to the interfacial strength, τ^0 , i.e., the maximum traction on the traction-displacement jump relation. When the area under the traction-displacement jump relation is equal to the fracture toughness, G_c , the traction is reduced to zero, and new crack surfaces are formed. There are several types of constitutive equations used in decohesion elements: Tvergaard and Hutchinson [16] proposed a

trapezoidal law, Cui and Wisnom [17] a perfectly plastic rule, Needleman first proposed a polynomial law, [18], and later an exponential law [19]. Goyal et al. [10] adopted Needleman's exponential law to account for load reversal without restoration of the cohesive state. The law used in this paper is a bilinear relation between the tractions and the displacement jumps [6],[9],[11],[12],[20], (see Figure 2).

[Figure 2 about here]

2.2 Cohesive zone model and FEM

In a finite element model using the CZM approach, the complete material description is separated into fracture properties captured by the constitutive model of the cohesive surface and the properties of the bulk material, captured by the continuum regions.

There are two conditions to obtain a successful FEM simulation using CZM [21]: (a) The cohesive contribution to the global compliance before crack propagation should be small enough to avoid the introduction of a fictitious compliance to the model, and (b) the element size needs to be less than the cohesive zone length.

(a) *Stiffness of the cohesive zone model*

Different guidelines have been proposed for selecting the stiffness of the interface. Daudeville et al. [23] calculated the stiffness in terms of the thickness and the elastic modulus of the interface. The resin-rich interface between plies

is of the order of 10^{-5}m . Therefore, the interface stiffness obtained from the Daudeville equations is very high. Zou et al. [24], based on their own experience, proposed a value for the interface stiffness between 10^4 and 10^7 times the value of the interfacial strength per unit length. Camanho and Dávila [9] obtained accurate predictions for Graphite/Epoxy specimens using a value of $10^6\text{N}/\text{mm}^3$.

The effective elastic properties of the whole laminate depend on the properties of both the cohesive surfaces and the bulk constitutive relations of the plies. Although the compliance of the cohesive surfaces can contribute to the global deformation, its only purpose is to simulate fracture. Moreover, the elastic properties of the cohesive surfaces are mesh-dependent because the surface relations exhibit an inherent length scale that is absent in homogeneous deformations [22].

If the cohesive contribution to the compliance is not small enough compared to that of the volumetric constitutive relation, a stiff connection between two neighboring layers before delamination initiation is not assured. The effect of compliance of the interface on the bulk properties of a laminate is illustrated in the one-dimensional model shown in Figure 3. The traction continuity condition requires:

$$\sigma = E_3\varepsilon = K\Delta \tag{4}$$

where σ is the traction on the surface, t is the thickness of an adjacent sublaminar, $\varepsilon = \frac{\delta t}{t}$ is the transverse strain, K is the interface stiffness that relates the resulting tractions at the interface with the opening displacement

Δ , and E_3 is the through-the-thickness Young's modulus of the material. For a transversely isotropic material $E_3 = E_2$.

[Figure 3 about here]

The effective strain of the composite is:

$$\varepsilon_{\text{eff}} = \frac{\delta t}{t} + \frac{\Delta}{t} = \varepsilon + \frac{\Delta}{t} \quad (5)$$

Since the traction continuity condition requires that $\sigma = E_{\text{eff}}\varepsilon_{\text{eff}}$, the equivalent Young's modulus E_{eff} can be written as a function of the Young's modulus of the material, the mesh size, and the interface stiffness. Using equations (4) and (5), the effective Young's modulus can be written as:

$$E_{\text{eff}} = E_3 \left(\frac{1}{1 + \frac{E_3}{Kt}} \right) \quad (6)$$

The effective elastic properties of the composite will not be affected by the cohesive surface whenever $E_3 \ll Kt$, i.e:

$$K = \frac{\alpha E_3}{t} \quad (7)$$

where α is a parameter much larger than 1 ($\alpha \gg 1$). However, large values of the interface stiffness may cause numerical problems, such as spurious oscillations of the tractions [4]. Thus, the interface stiffness should be large enough to provide a reasonable stiffness but small enough to avoid numerical problems such as spurious oscillations of the tractions in an element.

The ratio between the value of the Young modulus obtained with equation (6) and the Young modulus of the material, as a function of the parameter α is shown in Figure 4. For values of α greater than 50, the loss of stiffness due to the presence of the interface is less than 2%.

[Figure 4 about here]

The use of equation (7) is preferable to the guidelines presented in previous work [9],[23]-[24] because it results from mechanical considerations, and it provides a sufficient stiffness (α times the stiffness of the material) while avoiding spurious oscillations caused by an excessively stiff interface. The values of the interface stiffness obtained with equation (7) and those used by other authors for a carbon/epoxy composite are shown in Table 1. The material's transverse modulus is 11GPa, its nominal interfacial strength is $\tau^0 = 45\text{MPa}$, and α is taken as 50.

[Table 1 about here]

Equation (7) gives a range of the interface stiffness between 10^5 and $5 \times 10^6 \text{N/mm}^3$ for a sub-laminate thickness between 0.125mm and 5mm. These values are close to the interface stiffness proposed by Camanho and Dávila and the values obtained from Zou's guidelines (between 4.5×10^5 and $4.5 \times 10^8 \text{N/mm}^3$).

(b) *Length of the cohesive zone*

Under single-mode loading, interface damage initiates at a point where the traction reaches the maximum nominal interfacial strength, τ^0 . For mixed-mode loading, interface damage onset is predicted by a criterion established

in terms of the normal and shear tractions. Crack propagation occurs when the energy release rate reaches a critical value G_c . The CZM approach prescribes the interfacial normal and shear tractions that resist separation and relative sliding at an interface. The tractions, integrated to complete separation, yield the fracture energy release rate, G_c . The length of the cohesive zone l_{cz} is defined as the distance from the crack tip to the point where the maximum cohesive traction is attained (see Figure 5).

[Figure 5 about here]

Different models have been proposed in the literature to estimate the length of the cohesive zone. Irwin [25] estimated the size of the plastic zone ahead of a crack in a ductile solid by considering the crack tip zone within which the von Mises equivalent stress exceeds the tensile yield stress. Dugdale [13] estimated the size of the yield zone ahead of a mode I crack in a thin plate of an elastic-perfectly plastic solid by idealizing the plastic region as a narrow strip extending ahead of the crack tip that is loaded by the yield traction. Barenblatt [14] provided an analogue for ideally brittle materials of the Dugdale plastic yield zone analysis. Hui [26] estimated the length of the cohesive zone for soft elastic solids, and Falk [21] and Rice [27] estimated the length of the cohesive zone as a function of the crack growth velocity. The expressions that result from these models for the case of plane stress are presented in Table 2. It is assumed that the relation between the critical stress intensity factor K_c and the critical energy release rate G_c can be expressed as $K_c^2 = G_c E$.

All of the models described above to predict the cohesive zone length l_{cz} have the form:

$$l_{cz} = ME \frac{G_c}{(\tau^0)^2} \quad (8)$$

where E is the Young modulus of the material, G_c is the critical energy release rate, τ^0 is the maximum interfacial strength, and M is a parameter that depends on each model. The most commonly used models in the literature are Hillerborg's model [15] and Rice's model [27]. In these models, the parameter M is either close or exactly equal to unity. A summary of the different models commonly used in the literature, and the equivalent parameter M for plane stress are shown in Table 2. In this paper, Hillerborg's model is used in the following analysis.

For the case of orthotropic materials with transverse isotropy, the value of the Young's modulus in equation (8) is the transverse modulus of the material, E_2 .

[Table 2 about here]

In order to obtain accurate FEM results using CZM, the tractions in the cohesive zone must be represented properly by the finite element spatial discretization. The number of elements in the cohesive zone is:

$$N_e = \frac{l_{cz}}{l_e} \quad (9)$$

where l_e is the mesh size in the direction of crack propagation.

When the cohesive zone is discretized by too few elements, the fracture energy is not represented accurately and the model does not capture the continuum

field of a cohesive crack. Therefore, a minimum number of elements, N_e , is needed in the cohesive zone to get successful FEM results.

However, the minimum number of elements needed in the cohesive zone is not well established: Moës and Belytschko [28], based on the work of Carpinteri and Cornetti [29], suggest using more than 10 elements. However, Falk et al. [21] used between 2 and 5 elements in their simulations. In the parametric study by Dávila and Camanho [30], the minimum element length for predicting the delamination in a double cantilever beam (DCB) specimen was 1mm, which leads, using equation (8) with $M = 1$, to a length of the cohesive zone of 3.28mm. Therefore, 3 elements in the cohesive zone were sufficient to predict the propagation of delamination in Mode I.

2.3 Guidelines for the selection of the parameters of the interface with coarser meshes

One of the drawbacks in the use of cohesive zone models is that very fine meshes are needed to assure a reasonable number of elements in the cohesive zone. The length of the cohesive zone given by equation (8) is proportional to the fracture energy release rate (G_c) and to the inverse of the square of the interfacial strength τ^0 . For typical graphite-epoxy or glass-epoxy composite materials, the length of the cohesive zone is smaller than one or two millimeters. Therefore, according to equation (9), the mesh size required in order to have more than two elements in the cohesive zone should be smaller than half a millimeter. The computational requirements needed to analyze a large structure with these mesh sizes may render most practical problems intractable.

Alfano and Crisfield [8] observed that variations of the maximum interfacial strength do not have a strong influence in the predicted results, but that lowering the interfacial strength can improve the convergence rate of the solution. The result of using a lower interfacial strength is that the length of the cohesive zone and the number of elements in the cohesive zone increase. Therefore, the representation of the softening response of the fracture process ahead of the crack tip is more accurate with a lower interface strength although the stress distribution in the regions near the crack tip might be altered [8].

It is possible to develop a strategy to adapt the length of the cohesive zone to a given mesh size. The procedure consists of determining the value $\bar{\tau}^0$ of the interfacial strength required for a desired number of elements (N_e^0) in the cohesive zone. From equations (8) and (9), the required interface strength is:

$$\bar{\tau}^0 = \sqrt{\frac{EG_c}{N_e^0 l_e}} \quad (10)$$

Finally, the interfacial strength is chosen as:

$$T = \min \{ \tau^0, \bar{\tau}^0 \} \quad (11)$$

The interfacial strength is computed for each loading mode, replacing the value of the fracture toughness, G_c , in equation (10) by the value corresponding to the loading mode.

The effect of a reduction of the interfacial strength is to enlarge the cohesive zone, and thus, the model is better suited to capture the softening behaviour ahead of the crack tip. Moreover, if equation (7) is used to compute the interface stiffness, the interface stiffness will be large enough to assure a stiff

connection between the two neighboring layers and small enough to avoid spurious oscillations.

3 FEM implementation

The cohesive zone model used here is based on the model that was previously proposed by the authors [11]-[12]. The model has been adapted to be used in 2D finite element models. A brief description of the model, with special focus on the kinematics and constitutive damage model, is presented.

3.1 Kinematics and constitutive relation of cohesive zone models

The displacement jump across the interface of the material discontinuity required in the constitutive model, $\llbracket u_i \rrbracket$, can be obtained as a function of the displacement of the points located on the top and bottom side of the interface, u_i^+ and u_i^- , respectively:

$$\llbracket u_i \rrbracket = u_i^+ - u_i^- \quad (12)$$

where u_i^\pm are the displacements with respect to the fixed Cartesian coordinate system. A co-rotational formulation is used in order to express the components of the displacement jumps with respect to the deformed interface. The coordinates \bar{x}_i of the deformed interface can be written as [31]:

$$\bar{x}_i = X_i + \frac{1}{2} (u_i^+ + u_i^-) \quad (13)$$

where X_i are the coordinates of the undeformed interface.

The components of the displacement jump tensor in the local coordinate system on the deformed interface, Δ_m , are expressed in terms of the displacement field in global coordinates:

$$\Delta_m = \Theta_{mi} \llbracket u_i \rrbracket \quad (14)$$

where Θ_{mi} is the rotation tensor.

The constitutive operator of the interface, D_{ji} , relates the element tractions, τ_j , to the displacement jumps, Δ_i :

$$\tau_j = D_{ji} \Delta_i \quad (15)$$

A requirement of the constitutive relations of cohesive zone models is that the energy dissipated in the process of fracture needs to be computed accurately.

Under single-mode loading, controlled energy dissipation is achieved assuring that the area under the traction-displacement jump relation equals the corresponding fracture toughness, as illustrated in Figure 6.

[Figure 6 about here]

Under mixed-mode loading, a criterion established in terms of an interaction between components of the energy release rate needs to be used to predict crack propagation.

The constitutive damage model used here, formulated in the context of Damage Mechanics (DM), was previously proposed by the authors [11],[12]. All the details of the constitutive model are presented in references [11] and [12] and will not be repeated here. The formulation presented in previous references is adapted to use the decohesion elements together with 2D plane strain elements.

The constitutive model prevents interpenetration of the faces of the crack during closing, and a Fracture Mechanics-based criterion is used to predict crack propagation. The formulation of the damage model is summarized in Table 3, where ψ and ψ^0 are the free energy per unit surface of the damaged and undamaged interface, respectively. $\bar{\delta}_{ij}$ is the Kronecker delta, and \mathbf{d} is a scalar damage variable. The parameter λ is the norm of the displacement jump tensor (also called *equivalent displacement jump norm*), and it is used to compare different stages of the displacement jump state so that it is possible to define such concepts as ‘loading’, ‘unloading’ and ‘reloading’. The equivalent displacement jump is a non-negative and continuous function, defined as:

$$\lambda = \sqrt{\langle \Delta_1 \rangle^2 + (\Delta_2)^2} \quad (16)$$

where $\langle \cdot \rangle$ is the MacAuley bracket defined as $\langle x \rangle = \frac{1}{2}(x + |x|)$. Δ_1 is the displacement jump in mode I, i.e., normal to midplane, and Δ_2 is the displacement jump in mode II.

[Table 3 about here]

The evolution of damage is defined by $\mathbf{G}(\cdot)$, a suitable monotonic scalar function, ranging from 0 to 1. μ is a damage consistency parameter used to define

loading-unloading conditions according to the Kuhn-Tucker relations. r^t is the damage threshold for the current time, t , and r^0 denotes the initial damage threshold. The initial damage threshold is obtained from the formulation of the initial damage surface or initial damage criterion. Δ^0 is the onset displacement jump, and it is equal to the initial damage threshold r^0 . Δ^f is the final displacement jump, and it is obtained from the formulation of the propagation surface or propagation criterion. Further details regarding the damage model used here can be found in references [11]-[12].

4 Simulation of the double cantilever beam specimen

The influence of mesh size, interface stiffness, interface strength, and the selection of the parameters of the constitutive equation according to the proposed methodology were investigated by analyzing the Mode I delamination test (double cantilever beam, DCB). The DCB specimen was fabricated with a unidirectional T300/977-2 carbon-fiber-reinforced epoxy laminate. The specimen was 150-mm-long, 20.0 mm-wide, with two 1.98-mm-thick arms, and it had an initial crack length of 55mm. The material properties are shown in Table 4 [32].

[Table 4 about here]

The FEM model is composed of two layers of four-node 2D plane strain elements connected together with four-node decohesion elements. The decohesion elements were implemented using a user-written subroutine in the finite element code ABAQUS [33].

Three sets of simulations were performed. First, a DCB test was simulated with different levels of mesh refinement using the material properties shown in Table 4 and interfacial stiffness of $K=10^6\text{N/mm}^3$. Then, equations (9) and (7) were used to calculate an adjusted interfacial strength and interface stiffness. Finally, a set of simulations with a constant mesh size using different interface stiffnesses were performed in order to investigate the influence of the stiffness on the calculated results.

To study the effects of mesh refinement, several analyses were carried out for element sizes ranging between 0.125mm and 5mm. The corresponding load-displacement curves are shown in Figure 7. The results indicate that a mesh size of $l_e \leq 0.5\text{mm}$ is necessary to obtain converged solutions. The predictions made with coarser meshes overpredict significantly the experimental results. The length l_{cz} of the cohesive zone for the material given in Table 4 is close to 1mm. Therefore, for a mesh size greater than 0.5mm, fewer than two elements would span the cohesive zone, which is not sufficient for an accurate representation of the fracture process [29]-[30].

[Figure 7 about here]

4.1 *Effect of interface strength*

To verify the effect of the interface strength on the computed results, simulations were performed by specifying the desired number of elements within the cohesive zone to be $N_0 = 5$ and reducing the interface strength according to equation (11). The load-displacement curves obtained for several levels of

mesh refinement are shown in Figure 8. Accurate results are obtained for mesh sizes smaller than 2.5mm.

[Figure 8 about here]

[Figure 9 about here]

A comparison of the load-displacement curves for the DCB specimen calculated using the nominal interface strength and the strength obtained from equation (11) is shown in Figure 9. The specimen's failure load obtained by keeping the maximum interfacial strength constant increases with the mesh size. Mesh dependence is especially strong for mesh sizes greater than 2mm. However, the failure loads predicted by modifying the interfacial strength according to equation (11) are nearly constant for element sizes smaller than 3mm. In addition, the global deformation and the crack tip position are also nearly independent from mesh refinement, as illustrated in Figure 10.

[Figure 10 about here]

4.2 Effect of interface stiffness

The DCB test was simulated with a mesh size of 2.5mm for various values of the interface stiffness in order to investigate the influence of the stiffness

on the predicted failure load. The results of the simulations are presented in Figure 11.

The load-displacement response curves obtained from simulations using an interface stiffness greater than 10^4N/mm^3 are virtually identical. However, smaller values of the interface stiffness have a strong influence on the load-displacement curves, since a stiff connection between the two neighboring layers is not assured. Moreover, the number of iterations needed for the solution when using an interface stiffness smaller than 10^4N/mm^3 is greater than the number of iterations needed for a range of the interface stiffness between 10^6 and 10^{10}N/mm^3 . For values of the interface stiffness significantly greater than 10^{10}N/mm^3 , the number of iterations needed for the solution increases (see Figure 12). The stiffness that results from equation (7) with $\alpha = 50$ is $5.55 \times 10^5\text{N/mm}^5$, which is ideal for good convergence of the solution procedure.

[Figure 11 about here]

[Figure 12 about here]

5 Simulation of free-edge delamination

In order to demonstrate the mesh size effect and to further validate the accuracy of the methodology proposed, simulations were performed of the fracture

of specimens without initial cracks. One of the causes of the initiation of delamination in specimens without initial cracks is the effect of free edge stress distributions. Delamination induced by the free-edge effect was investigated by many authors [34]-[36].

5.1 *Problem statement*

Crossman et al. investigated the free edge effects in a $[+25/-25/90]_s$ graphite-epoxy laminate subjected to uniaxial strain [35]. The laminates were fabricated from Fiberite T300/934 prepreg tape using an autoclave. The cross-section of the specimen was 25.0-mm-wide and 0.792-mm-thick (see Figure 13). No initial cracks were induced in the laminate. The material properties are shown in Table 5 [34],[37].

Tensile tests were performed by applying a controlled displacement in the x-direction. Due to the stacking sequence, the through the thickness free-edge stress distribution produces high σ_{zz} in the 90° ply. Therefore, important tractions occur at the $90^\circ/90^\circ$ interface, leading to the onset of delamination at the free-edge.

[Figure 13 about here]

[Table 5 about here]

5.2 Numerical predictions

A FEM model was developed using six layers of 4-node generalized plane strain elements [38]. The $90^\circ/90^\circ$ interface was modelled with 4-node decohesion elements presented in previous sections. The elastic properties of each layer were defined by means of the 3D stiffness matrix. The decohesion elements were implemented using a user-written subroutine in the finite element code ABAQUS [33]. Due to the symmetry of the laminate, only half of the cross-section was modelled.

Two sets of simulations were performed. First, tensile tests were simulated with different levels of mesh refinement. Then, equations (9) and (7) were used to calculate the interface strength and the interface stiffness.

Several analyses were carried out for mesh sizes ranging between 0.05mm and 0.5mm. The load-displacement curves obtained are shown in Figure 14. An interfacial stiffness of $K=10^6\text{N/mm}^3$, an interface strength of 51.7MPa, a critical energy release rate of 0.175N/mm [34], and the material properties shown in Table 5 were used. The length of the cohesive zone obtained with these properties, using equation (8), is 0.361mm. A mesh size smaller than 0.1mm is needed in order to have three or more elements in the cohesive zone. The predictions obtained using different levels of mesh refinement are shown in Figure 14. Using meshes coarser than 0.1mm, the correct solution is significantly overpredicted. For a mesh size greater than 0.5mm the maximum applied load is greater than two times the maximum load obtained with meshes smaller than 0.1mm.

[Figure 14 about here]

The ultimate tensile strength calculated using a mesh size of 0.1mm is 404MPa. Delamination onset occurs when a point in the interface is not able to carry any traction, which changes the stress distribution. The stress maps in a plane perpendicular to the interface and normal to the load direction are represented in Figure 15 for three stages of deformation. At the first stage, before delamination onset, the stresses near the free edge are tensile due to the mismatch effect of the Poisson ratio (black zones in Figure 15). At delamination onset, a region of the free edge is unable to carry load and the stresses become compressive, as shown in Figure 15b). The predicted onset of delamination is $\varepsilon_{xx} = 0.6\%$, and the corresponding stress is 392MPa. The experimental results obtained by Crossman and Wang [35] reported a delamination onset tensile stress of 409MPa and an ultimate tensile strength of 459MPa. The predicted and experimental onset and failure stresses and strains are summarized in Table 6. Unstable delamination propagation and the corresponding structural collapse occurs at a strain of 0.6183%.

[Figure 15 about here]

[Table 6 about here]

To verify the effect of interface strength on the predicted results, simulations were performed by specifying the desired number of elements spanning the cohesive zone to be $N_0 = 5$ and reducing the interface strength according to equation (11). The load-displacement curves obtained for several levels of mesh refinement are shown in Figure 16. A comparison of the maximum load obtained using the nominal interface strength and the strength obtained from

equation (11) is shown in Figure 17. Accurate predictions are obtained using the modified interface strength instead of the nominal interface strength.

[Figure 16 about here]

[Figure 17 about here]

A similar study of mesh size effect was repeated by the desired number of elements spanning the cohesive zone to be $N_0 = 10$. Although the results presented in Figures 18 and 19 are more accurate than those for $N_0 = 5$, the improvement is insignificant.

[Figure 18 about here]

[Figure 19 about here]

6 Concluding remarks

An engineering solution for the simulation of delamination using coarse meshes was developed. Two new guidelines for the selection of the parameters for the constitutive equation used for the simulation of delamination were presented.

First, a new equation for the selection of the interface stiffness parameter K was derived. The new equation is preferable to previous guidelines because it results from mechanical considerations rather than from experience. The approach provides an adequate stiffness to ensure a sufficiently stiff connection between two neighboring layers, while avoiding the possibility of spurious oscillations in the solution caused by overly stiff connections.

Finally, an expression to adjust the maximum interfacial strength used in the computations with coarse meshes was presented. It was shown that a minimum number of elements within the cohesive zone is necessary for accurate simulations. By reducing the maximum interfacial strength, the cohesive zone length is enlarged and more elements span the cohesive zone. The results obtained by reducing the maximum interfacial strength show that accurate results can be obtained with a mesh ten times coarser than by using the nominal interface strength. The drawback in using a reduced interfacial strength value is that the stress concentrations in the bulk material near the crack tip are less accurate.

7 Acknowledgments

This work has been partially funded by the Spanish government through DG-ICYT under contract: MAT2003-09768-C03-01. The first author would like to thank you the University of Girona for the grant BR01/09.

References

- [1] Krueger, R., The virtual crack closure technique: history, approach and applications. *NASA/Contractor Report-2002-211628*, 2002.
- [2] Allix, O., Ladeveze, P., Corigliano, A., Damage analysis of interlaminar fracture specimens. *Composite Structures* **31**, 66-74, 1995.
- [3] Allix, O., Corigliano, A., Modelling and simulation of crack propagation in mixed-modes interlaminar fracture specimens. *International Journal of Fracture* **77**,111-140, 1996.
- [4] Schellekens, J.C.J., de Borst, R., A nonlinear finite-element approach for the analysis of mode-I free edge delamination in composites. *International Journal for Solids and Structures*, **30**(9), 1239-1253, 1993.
- [5] Chaboche, J.L., Girard, R., Schaff, A., Numerical analysis of composite systems by using interphase/interface models. *Computational Mechanics*. **20**, 3-11, 1997.
- [6] Mi, U., Crisfield, M.A., Davies, G.A.O., Progressive delamination using interface elements. *Journal of Composite Materials*, **32**, 1246-1272, 1998.
- [7] Chen, J., Crisfield, M.A., Kinloch, A.J., Busso, E.P., Matthews, F.L., and Qiu, Y., Predicting progressive delamination of composite material specimens via interface elements. *Mechanics of Composite Materials and Structures*, **6**, 301–317, 1999.
- [8] Alfano, G., Crisfield, M.A., Finite element interface models for the delamination analysis of laminated composites: mechanical and computational issues. *International Journal for Numerical Methods in Engineering*, **77**(2), 111-170, 2001.
- [9] Camanho, P.P., Dávila, C.G., de Moura, M.F., Numerical simulation of mixed-mode progressive delamination in composite materials. *Journal of Composite*

Materials, **37** (16), 1415-1438, 2003.

- [10] Goyal-Singhal, V., Johnson, E.R., Dávila, C.G., Irreversible constitutive law for modeling the delamination process using interfacial surface discontinuities. *Composite Structures*, **64**, 91-105, 2004.
- [11] Turon, A., Camanho, P.P., Costa, J., Dávila, C.G., An interface damage model for the simulation of delamination under variable-mode ratio in composite materials. *NASA/Technical Memorandum 213277*, 2004.
- [12] Turon, A., Camanho, P.P., Costa, J., Dávila, C.G., A damage model for the simulation of delamination in advanced composites under variable-mode loading. *Mechanics of Materials*, submitted, 2005.
- [13] Dugdale, D.S., Yielding of steel sheets containing slits. *Journal of the Mechanics and Physics of Solids* **8**, 100-104. 1960.
- [14] Barenblatt, G., The mathematical theory of equilibrium cracks in brittle fracture. *Advances in Applied Mechanics*, **7**, 55-129. 1962.
- [15] Hillerborg, A., Modéer, M., Petersson, P.E., Analysis of crack formation and crack growth in concrete by means of fracture mechanics and finite elements. *Cement and Concrete Research*. **6**, 773-782. 1976.
- [16] Tvergaard, V., Hutchinson, J.W., The relation between crack growth resistance and fracture process parameters in elastic-plastic solids. *Journal of Mechanics and Physics of Solids*, **40**, 1377-1397, 1992.
- [17] Cui, W., Wisnom, M.R., A combined stress-based and fracture-mechanics-based model for predicting delamination in composites. *Composites*, **24**, 467-474, 1993.
- [18] Needleman, A., A continuum model for void nucleation by inclusion debonding. *Journal of Applied Mechanics*, **54**, 525-532, 1987.

- [19] Xu X-P, Needleman, A., Numerical simulations of fast crack growth in brittle solids. *Journal of Mechanics and Physics of Solids*, **42** (9), 1397-1434, 1994.
- [20] Reddy Jr., E.D., Mello, F.J., Guess, T.R., Modeling the initiation and growth of delaminations in composite structures. *Journal of Composite Materials*, **31**, 812-831, 1997.
- [21] Falk, M.L., Needleman, A., Rice J.R., A critical evaluation of cohesive zone models of dynamic fracture. *Journal de Physique IV, Proceedings*, 543-550, 2001.
- [22] Klein, P.A., Foulk, J.W., Chen, E.P., Wimmer, S.A., Gao, H., Physics-based modeling of brittle fracture: cohesive formulations and the application of meshfree methods. *Sandia Report SAND2001-8099*, 2000.
- [23] Daudeville, L., Allix, O., Ladevèze, P., Delamination analysis by damage mechanics. Some applications. *Composites Engineering*, **5**(1), 17-24, 1995.
- [24] Zou, Z., Reid, S.R., Li, S., Soden, P.D., Modelling interlaminar and intralaminar damage in filament wound pipes under quasi-static indentation. *Journal of Composite Materials*, **36**, 477-499, 2002.
- [25] Irwin, G.R., Plastic zone near a crack and fracture toughness. In *Proceedings of the Seventh Sagamore Ordnance Materials Conference*, vol. **IV**, 63-78, New York: Syracuse University, 1960.
- [26] Hui, C.Y., Jagota, A., Bennison, S.J., Londono, J.D., Crack blunting and the strength of soft elastic solids. *Proceedings of the Royal Society of London A*, **459**, 1489-1516, 2003.
- [27] Rice, J.R., The mechanics of earthquake rupture. *Physics of the Earth's Interior (Proc. International School of Physics "Enrico Fermi", Course 78, 1979; ed. A.M. Dziewonski and E. Boschi)*, Italian Physical Society and North-Holland Publ. Co., 555-649, 1980.

- [28] Moës, N., Belytschko, T., Extended finite element method for cohesive crack growth. *Engineering Fracture Mechanics*, **69**,813-833, 2002.
- [29] Carpinteri, A., Cornetti, P., Barpi, F., Valente, S., Cohesive crack model description of ductile to brittle size-scale transition: dimensional analysis vs. renormalization group theory. *Engineering Fracture Mechanics*, **70**, 1809-1939, 2003.
- [30] Dávila, C.G., Camanho, P.P., de Moura, M.F.S.F., Mixed-Mode decohesion elements for analyses of progressive delamination. *Proceedings of the 42nd AIAA/ASME/ASCE/AHS/ASC Structures, Structural Dynamics and Materials Conference*, Seattle, Wasington, April 16-19, 2001.
- [31] Ortiz, M., Pandolfi, A., Finite-deformation irreversible cohesive elements for three-dimensional crack propagation analysis. *International Journal for Numerical Methods in Engineering*, **44**, 1267-82, 1999.
- [32] Morais, A.B., de Moura, M.F., Marques, A.T., de Castro, P.T., Mode-I interlaminar fracture of carbon/epoxy cross-ply composites. *Composites Science and Technology*, **62**, 679-686, 2002.
- [33] Hibbitt, Karlsson, Sorensen. ABAQUS 6.2 User's Manuals. Pawtucket, USA, 1996.
- [34] Schellekens, J.C.J., de Borst, R., Numerical simulation of free edge delamination in graphite-epoxy laminates under uniaxial tension, *6th International Conference on Composite Structures*, 647-657, 1991.
- [35] Crossman, F.W., Wang, A.S.D., The dependence of transverse cracking and delamination on ply thickness in graphite/epoxy laminates. *Damage in Composite Materials*, ed. K.L. Reifsnider, American Society for Testing and Materials (ASTM STP 775), Ann Arbor, Michigan, 118-39, 1982.

- [36] O'Brien, T.K., Characterization of delamination onset and growth in a composite laminate, *Damage in Composite Materials*, ed. K.L. Reifsnider, American Society for Testing and Materials (ASTM STP 775), Ann Arbor, Michigan, 140-67, 1982.
- [37] Wang, A.S.D., Fracture analysis of interlaminar cracking, *Interlaminar Response of Composite Materials*, Ed. N.J. Pagano, Elsevier Science Publishers BV, Amsterdam, 69-109, 1989.
- [38] Li, S., Lim, S.H., Variational principles for generalized plane strain problems and their applications, *Composites: Part A*, **36**, 353-365, 2005.

List of Figures

1	<i>Body Ω crossed by a material discontinuity Γ_d in the undeformed configuration.</i>	33
2	<i>Bilinear constitutive equation.</i>	34
3	<i>Influence of the cohesive surface on the deformation.</i>	35
4	<i>Ratio between the equivalent elastic modulus and the Young's modulus of the material, as a function of the parameter α.</i>	36
5	<i>Length of the cohesive zone.</i>	37
6	<i>Constitutive equations under Mode I and Mode II loading.</i>	38
7	<i>Load-displacement curves using the nominal interace strength ($\tau^0=60\text{MPa}$) for a DCB test with different mesh sizes.</i>	39
8	<i>Load-displacement curves obtained for a DCB test with different mesh sizes with the interface strength modified to keep $N_e \geq 5$.</i>	40
9	<i>Maximum load obtained in a DCB test for two cases: a) with constant interfacial strength, b) with interfacial strength calculated according to Eq. (11).</i>	41
10	<i>Comparison of crack tip position for two different levels of mesh refinement.</i>	42

11	<i>Influence of the interface stiffness on the load-displacement curves.</i>	43
12	<i>Influence of the interface stiffness on the number of iterations.</i>	44
13	<i>Cross-section of the laminate.</i>	45
14	<i>Load-displacement curves obtained for a free-edge test with different mesh sizes using nominal interface strength properties.</i>	46
15	<i>Evolution of stresses during delamination onset and propagation.</i>	47
16	<i>Load-displacement curves obtained for a free-edge test with different mesh sizes and with the interface strength adjusted for $N_e = 5$.</i>	48
17	<i>Maximum load obtained in a free-edge test for two cases: a) with constant interfacial strength, b) with interfacial strength calculated according to Eq.(11) with $N_e = 5$.</i>	49
18	<i>Load-displacement curves obtained for a free-edge test with different mesh sizes and with the interface strength adjusted for $N_e = 10$.</i>	50
19	<i>Maximum load obtained in a free-edge test for two cases: a) with constant interfacial strength, b) with interfacial strength calculated according to Eq.(11) with $N_e = 10$.</i>	51

List of Tables

1	Interface stiffness K proposed by different authors (N/mm^3) and those calculated from equation (7).	52
2	Length of the cohesive zone and equivalent value of the parameter M .	53
3	Definition of the constitutive model.	54
4	Mechanical and interface material properties of T300/977-2 [32].	55
5	Mechanical properties of T300/934 Graphite Epoxy [34], [37].	56
6	Summary of predicted and experimental values of tension tests on T300/934 laminates.	57

Figures

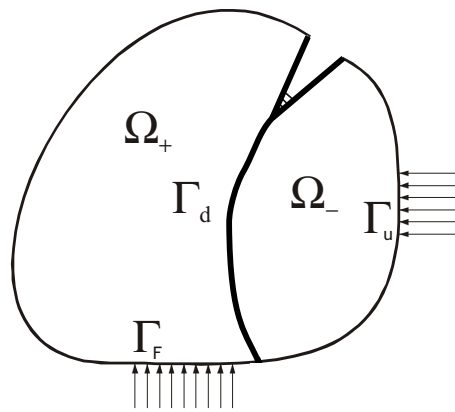


Fig. 1. *Body Ω crossed by a material discontinuity Γ_d in the undeformed configuration.*

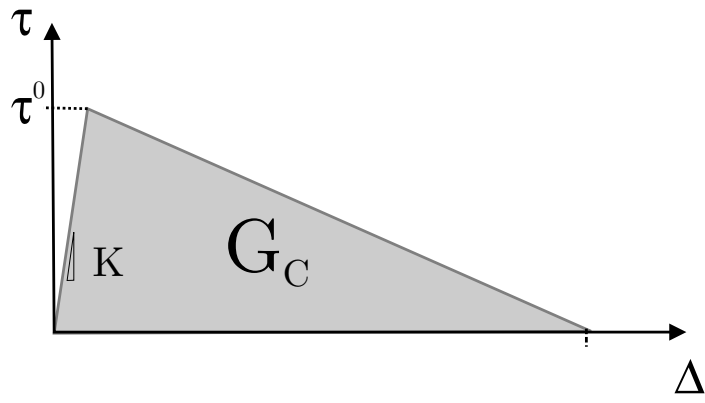


Fig. 2. *Bilinear constitutive equation.*

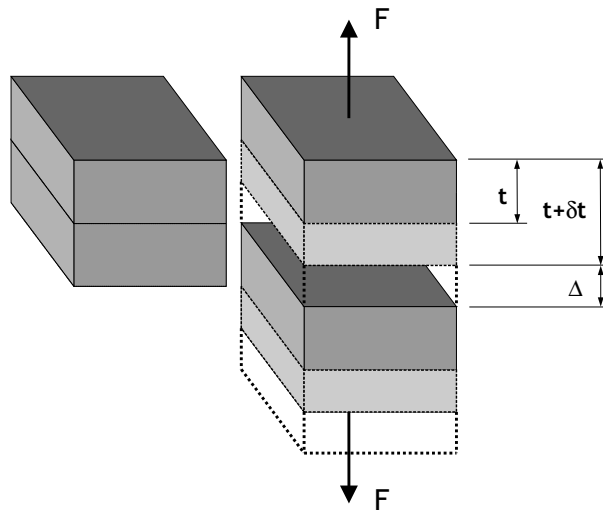


Fig. 3. *Influence of the cohesive surface on the deformation.*

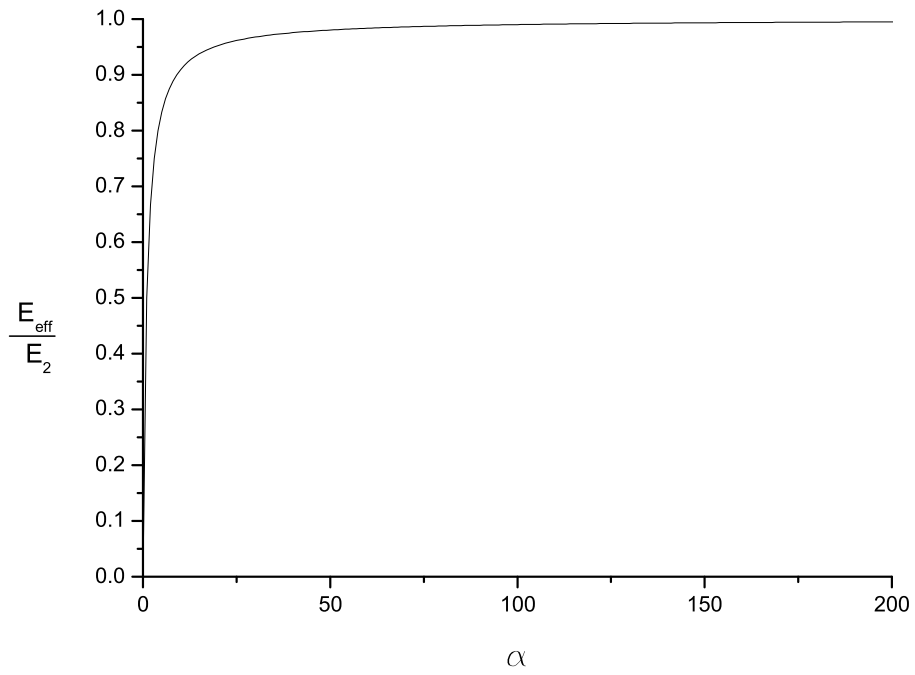


Fig. 4. Ratio between the equivalent elastic modulus and the Young's modulus of the material, as a function of the parameter α .

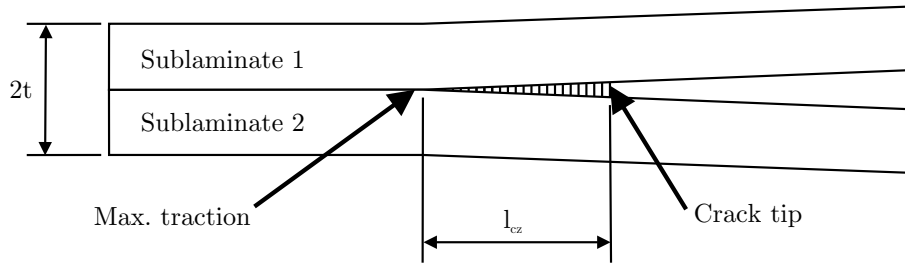


Fig. 5. *Length of the cohesive zone.*

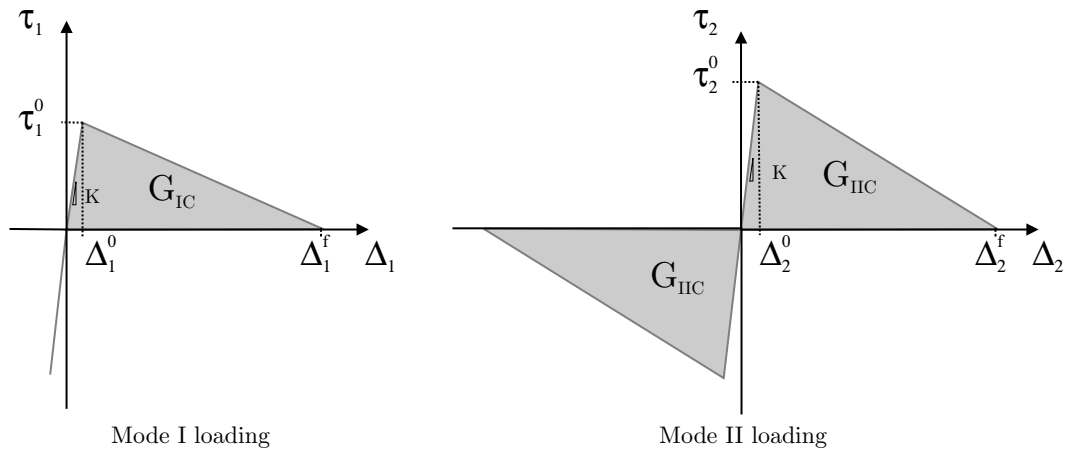


Fig. 6. Constitutive equations under Mode I and Mode II loading.

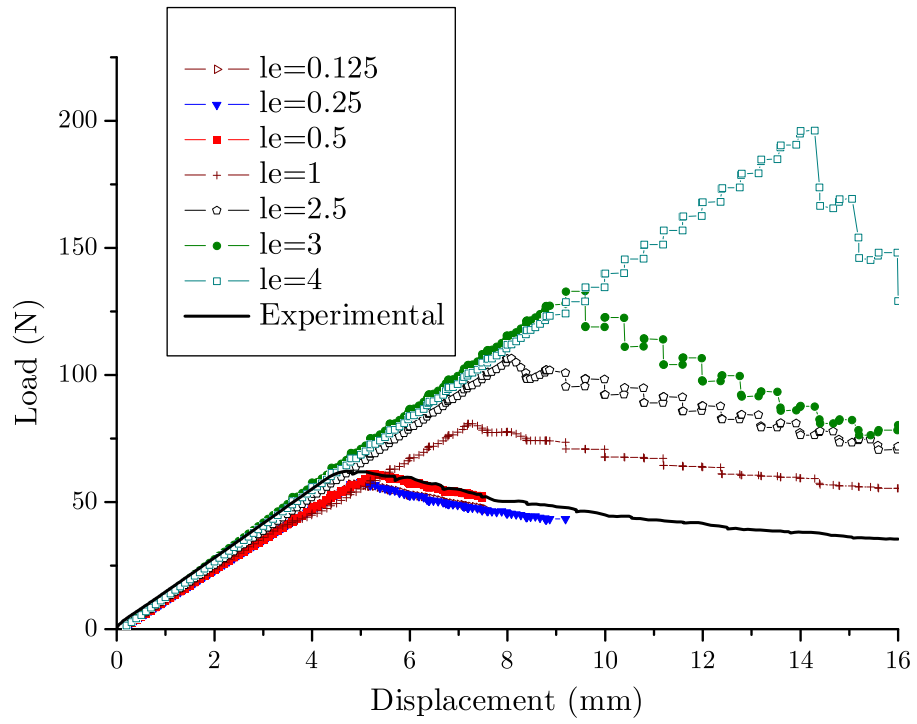


Fig. 7. Load-displacement curves using the nominal interfacial strength ($\tau^0=60\text{MPa}$) for a DCB test with different mesh sizes.

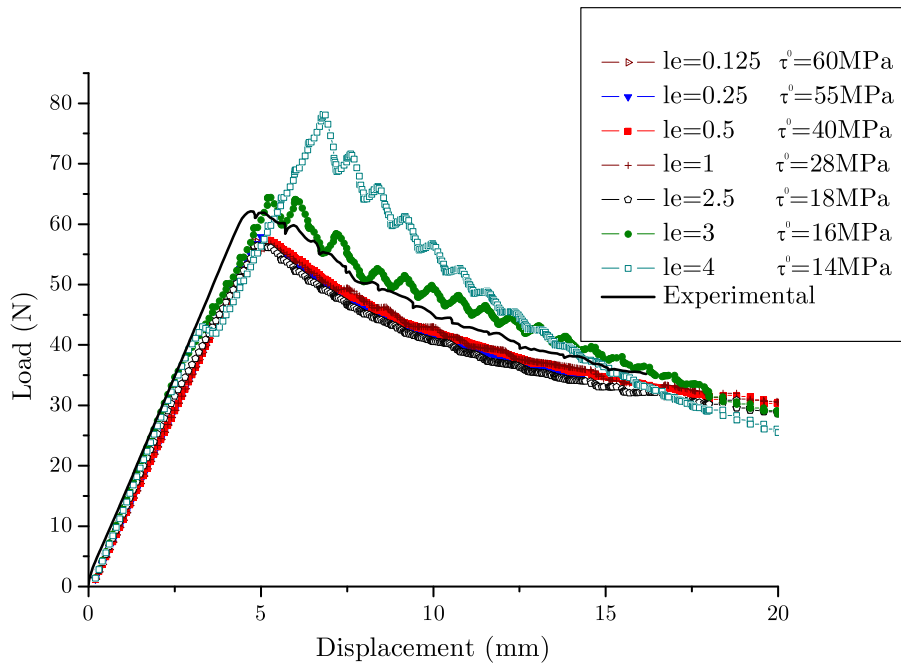


Fig. 8. Load-displacement curves obtained for a DCB test with different mesh sizes with the interface strength modified to keep $N_e \geq 5$.

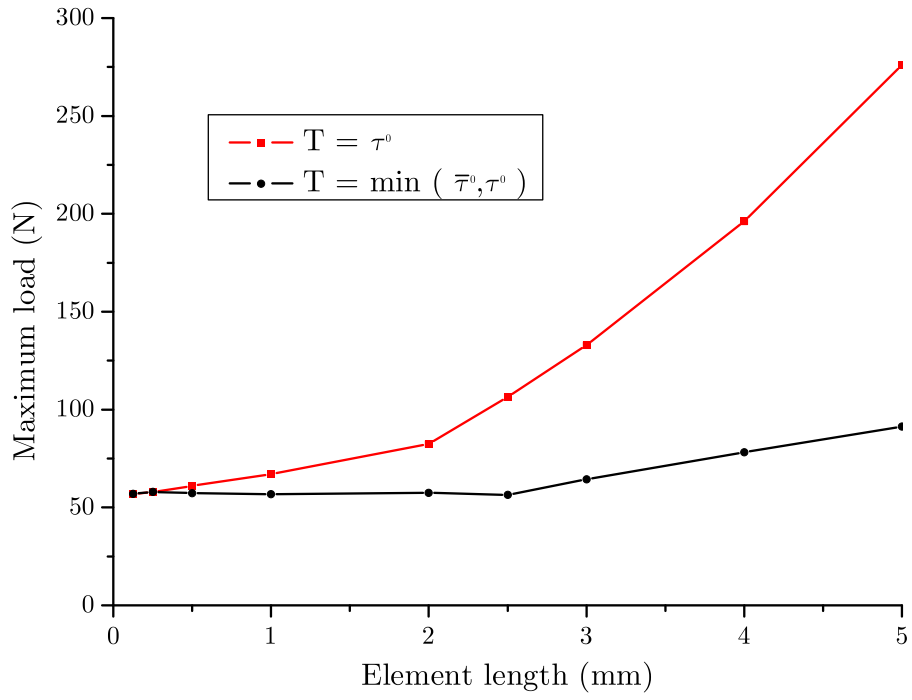


Fig. 9. Maximum load obtained in a DCB test for two cases: a) with constant interfacial strength, b) with interfacial strength calculated according to Eq. (11).

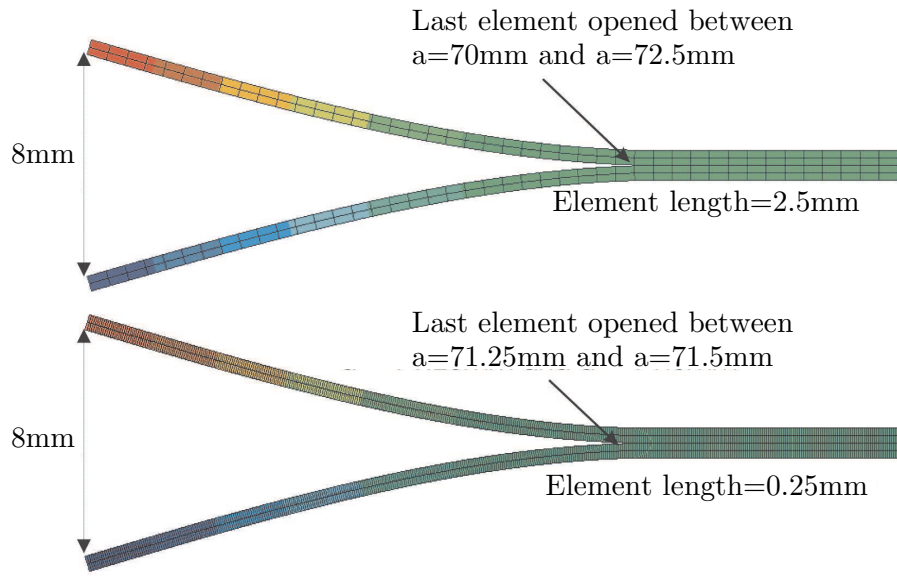


Fig. 10. Comparison of crack tip position for two different levels of mesh refinement.

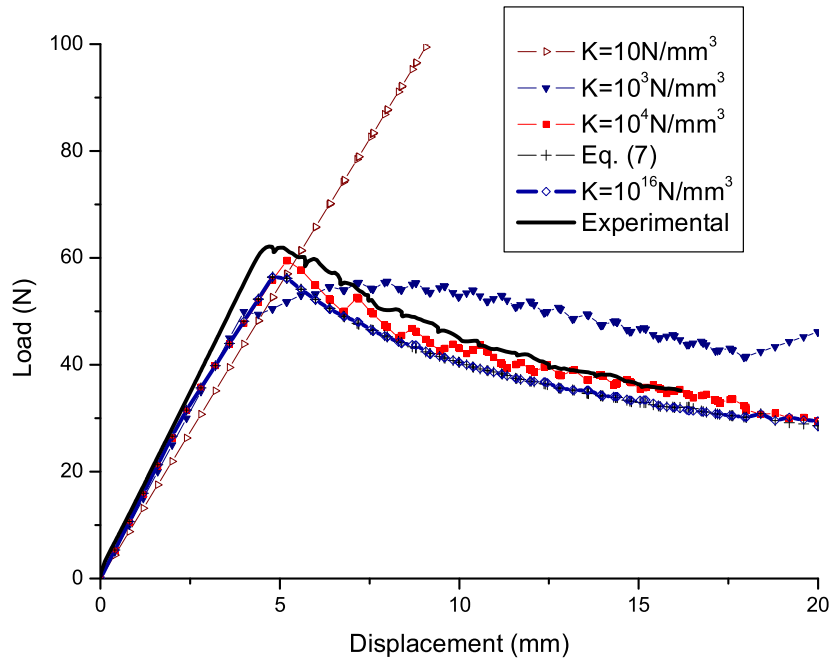


Fig. 11. Influence of the interface stiffness on the load-displacement curves.

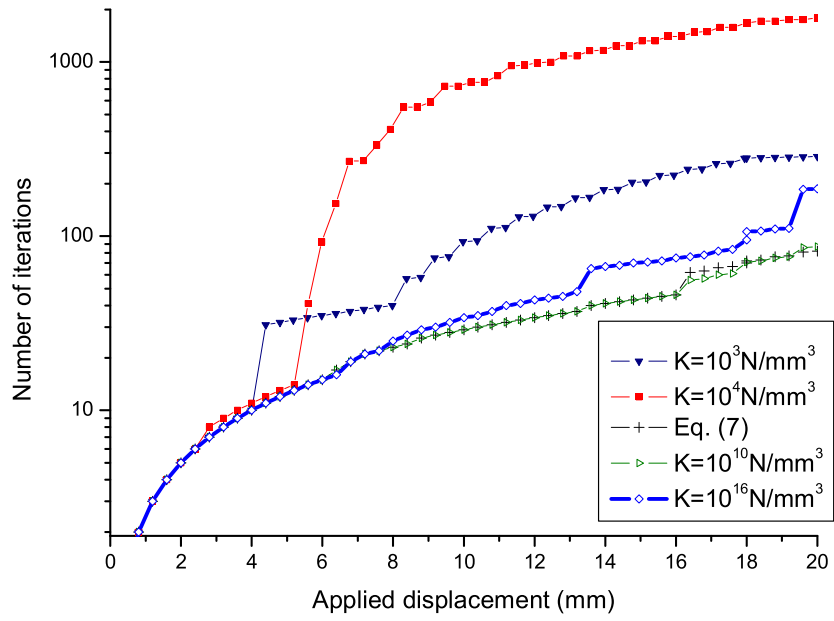


Fig. 12. Influence of the interface stiffness on the number of iterations.

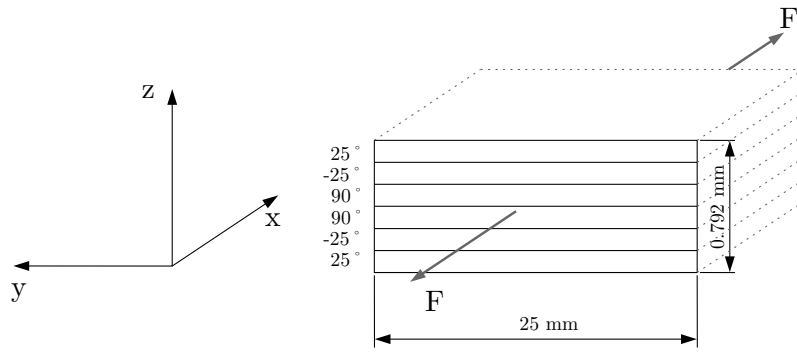


Fig. 13. *Cross-section of the laminate.*

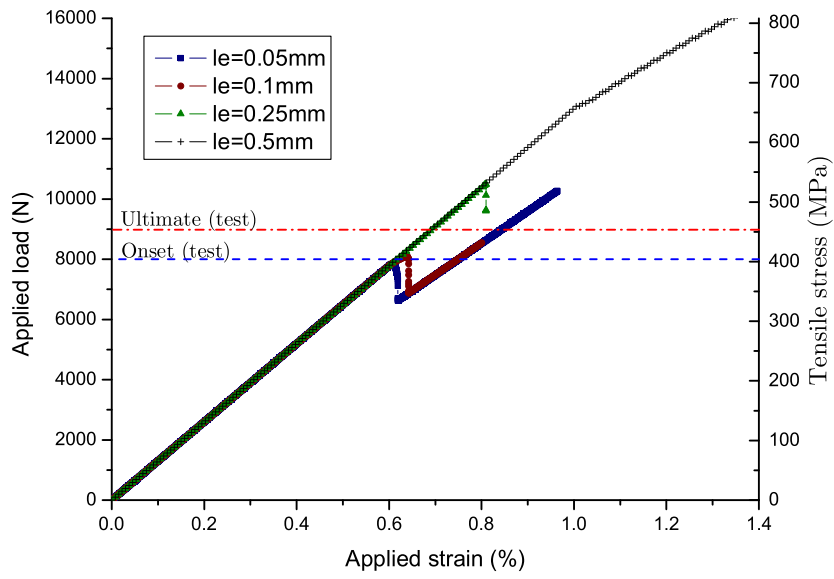


Fig. 14. Load-displacement curves obtained for a free-edge test with different mesh sizes using nominal interface strength properties.

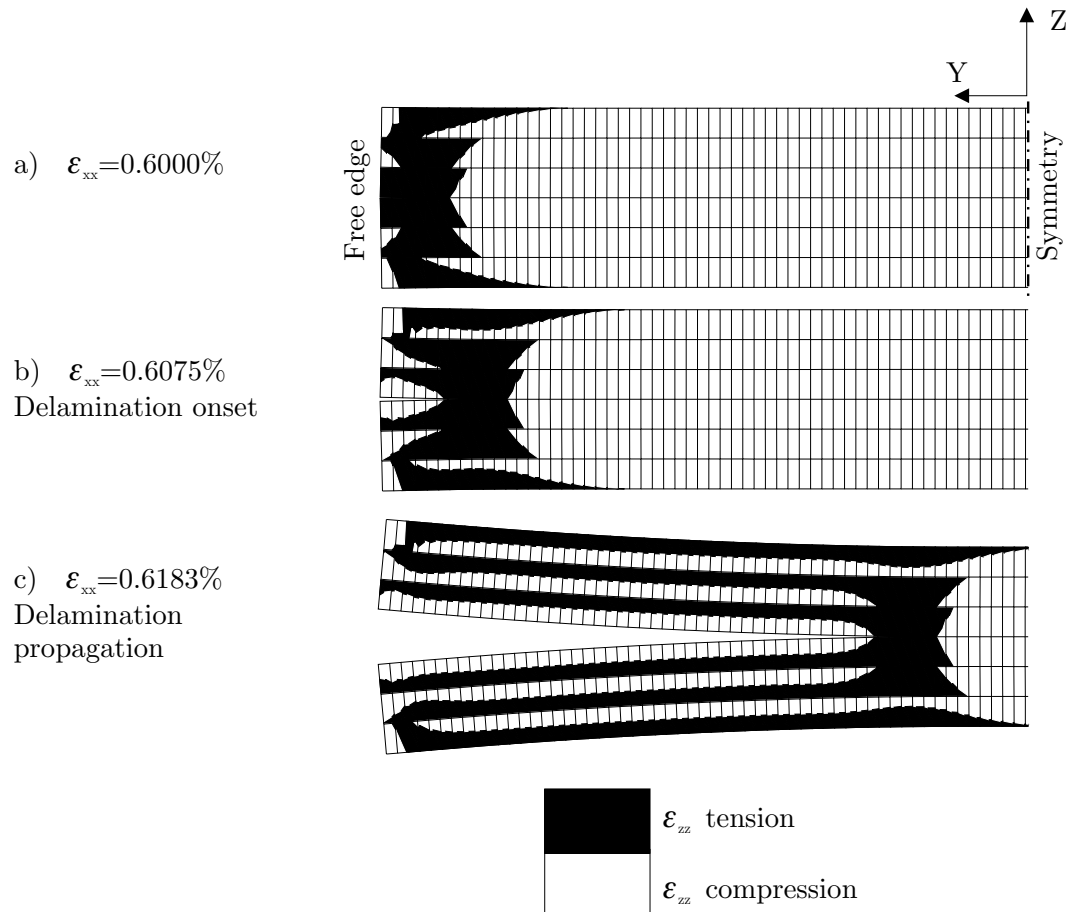


Fig. 15. *Evolution of stresses during delamination onset and propagation.*

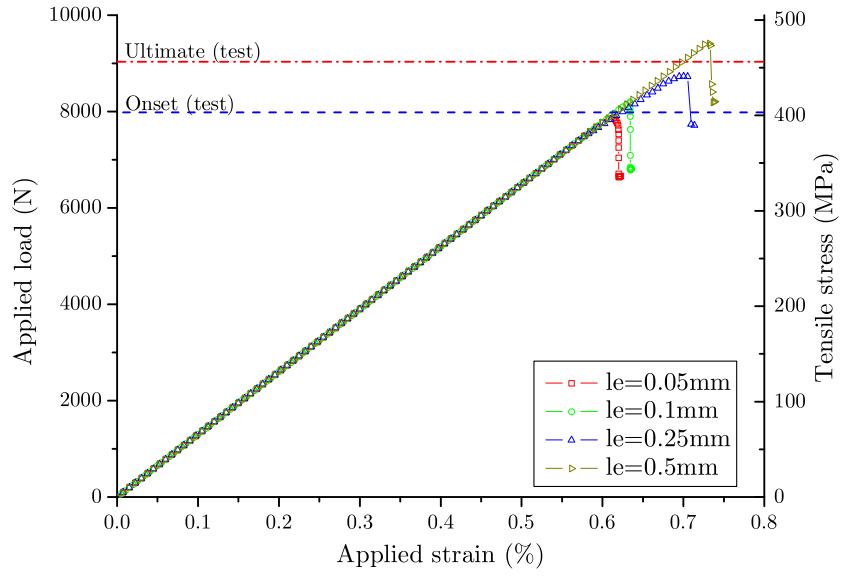


Fig. 16. Load-displacement curves obtained for a free-edge test with different mesh sizes and with the interface strength adjusted for $N_e = 5$.

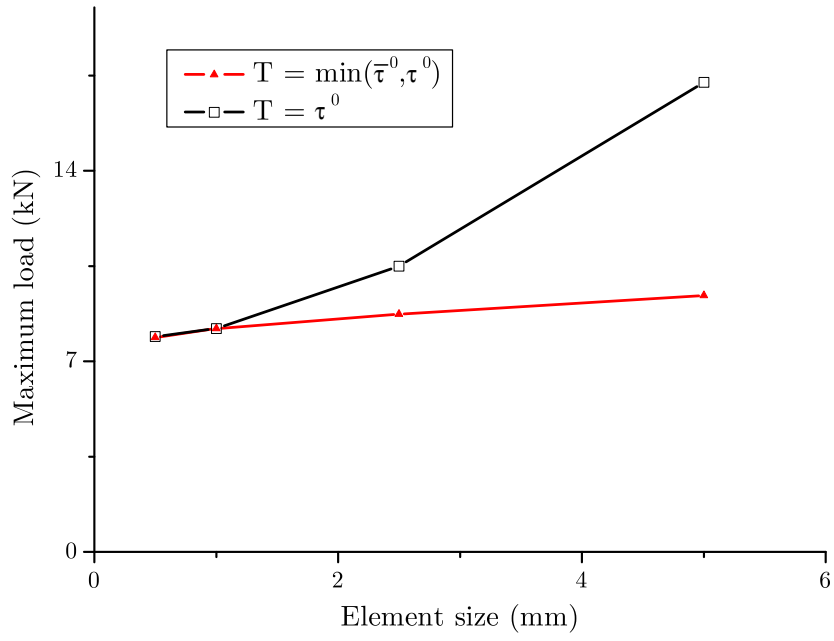


Fig. 17. Maximum load obtained in a free-edge test for two cases: a) with constant interfacial strength, b) with interfacial strength calculated according to Eq.(11) with $N_e=5$.

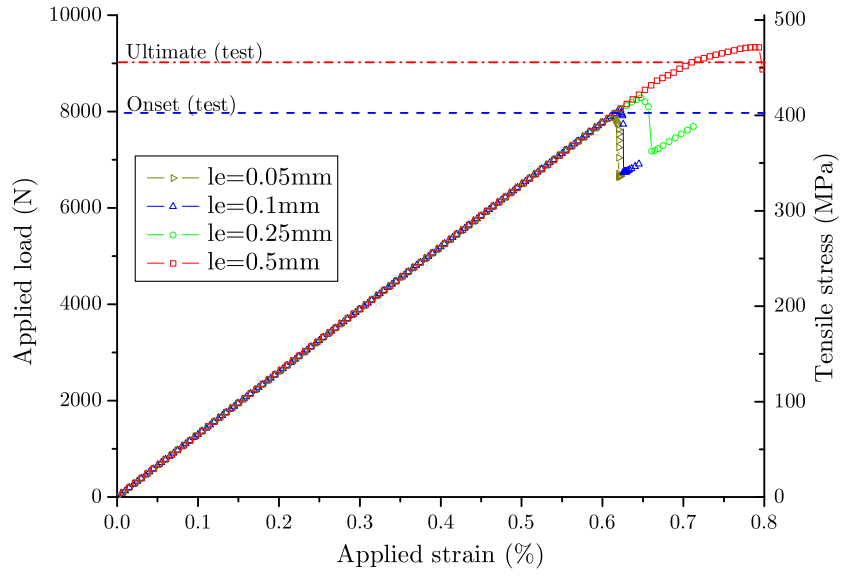


Fig. 18. Load-displacement curves obtained for a free-edge test with different mesh sizes and with the interface strength adjusted for $N_e = 10$.

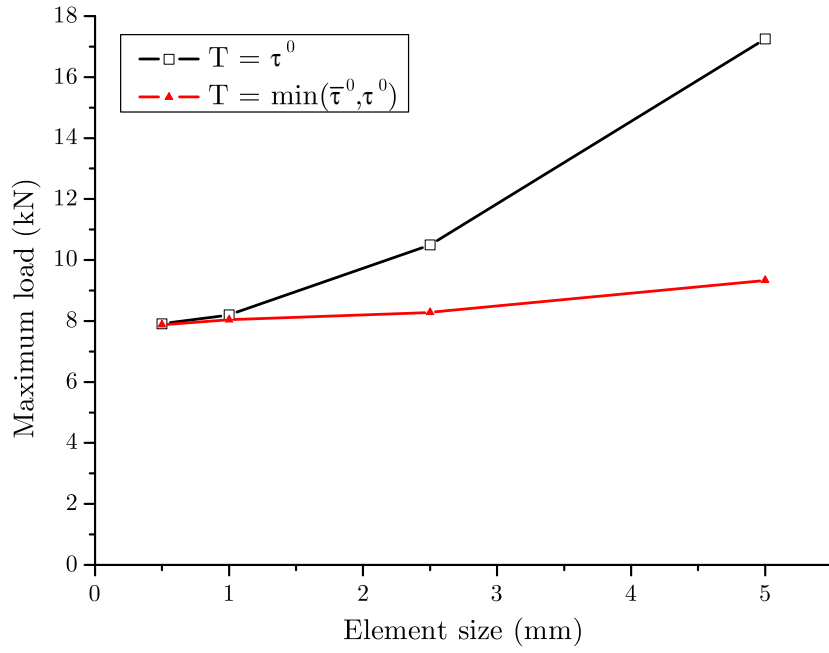


Fig. 19. Maximum load obtained in a free-edge test for two cases: a) with constant interfacial strength, b) with interfacial strength calculated according to Eq.(11) with $N_e=10$.

Tables

Table 1

Interface stiffness K proposed by different authors (N/mm^3) and those calculated from equation (7).

$t(mm)$	0.125	1	2	3	5
Equation (7)	4.43×10^6	5.5×10^5	2.75×10^5	1.83×10^5	1.1×10^5
Zou et al. [24]		4.5×10^5	$\leq K \leq$	4.5×10^8	
Camanho and Dávila [9]	10^6	10^6	10^6	10^6	10^6

Table 2

Length of the cohesive zone and equivalent value of the parameter M.

	l_{cz}	M
Hui [26]	$\frac{2}{3\pi} E \frac{G_c}{(\tau^0)^2}$	0.21
Irwin [25]	$\frac{1}{\pi} E \frac{G_c}{(\tau^0)^2}$	0.31
Dugdale [13], Barenblatt [14]	$\frac{\pi}{8} E \frac{G_c}{(\tau^0)^2}$	0.4
Rice [27], Falk [21]	$\frac{9\pi}{32} E \frac{G_c}{(\tau^0)^2}$	0.88
Hillerborg [15]	$E \frac{G_c}{(\tau^0)^2}$	1

Table 3

Definition of the constitutive model.

Free Energy	$\psi(\Delta, \mathbf{d}) = (1 - \mathbf{d}) \psi^0(\Delta_i) - \mathbf{d} \psi^0(\bar{\delta}_{1i} \langle -\Delta_1 \rangle)$
-------------	---------------------------------------------------------------------------------------------------------------------------------

Constitutive equation	$\tau_i = \frac{\partial \psi}{\partial \Delta_i} = (1 - \mathbf{d}) \bar{\delta}_{ij} K \Delta_j - \mathbf{d} \bar{\delta}_{ij} K \bar{\delta}_{1j} \langle -\Delta_1 \rangle$
-----------------------	---------------------------------------------------------------------------------------------------------------------------------------------------------------------------------

Displacement jump norm	$\lambda = \sqrt{\langle \Delta_1 \rangle^2 + (\Delta_2)^2}$
------------------------	--------------------------------------------------------------

Damage criterion	$\bar{F}(\lambda^t, r^t) := \mathbf{G}(\lambda^t) - \mathbf{G}(r^t) \leq 0 \quad \forall t \geq 0$
------------------	----------------------------------------------------------------------------------------------------

$$\mathbf{G}(\lambda) = \frac{\Delta^f (\lambda - \Delta^0)}{\lambda (\Delta^f - \Delta^0)}$$

Evolution law	$\dot{\mathbf{d}} = \dot{\mu} \frac{\partial \bar{F}(\lambda, r)}{\partial \lambda} = \dot{\mu} \frac{\partial \mathbf{G}(\lambda)}{\partial \lambda} \quad ; \quad \dot{r} = \dot{\mu}$
---------------	------------------------------------------------------------------------------------------------------------------------------------------------------------------------------------------

Load/unload conditions	$\dot{\mu} \geq 0 \quad ; \quad \bar{F}(\lambda^t, r^t) \leq 0 \quad ; \quad \dot{\mu} \bar{F}(\lambda^t, r^t) = 0$
------------------------	---------------------------------------------------------------------------------------------------------------------

$$r^t = \max \{ r^0, \max_s \lambda^s \} \quad 0 \leq s \leq t$$

Table 4

Mechanical and interface material properties of T300/977-2 [32].

E_{11}	$E_{22} = E_{33}$	$G_{12} = G_{13}$	G_{23}
150.0GPa	11.0GPa	6.0GPa	3.7GPa
$\nu_{12} = \nu_{13}$	ν_{23}	G_{IC}	τ_3^0
0.25	0.45	0.352N/mm	60MPa

Table 5

Mechanical properties of T300/934 Graphite Epoxy [34], [37].

E_{11}	$E_{22} = E_{33}$	$G_{12} = G_{13}$	G_{23}	$\nu_{12} = \nu_{13}$	ν_{23}
140.0GPa	11.0GPa	5.5GPa	3.61GPa	0.29	0.52

Table 6

Summary of predicted and experimental values of tension tests on T300/934 laminates.

	Predicted	Experimental	Difference
Strain at delamination onset (%)	0.6	0.59	2%
Stress at delamination onset (MPa)	392	404	-3%
Ultimate strain (%)	0.6183	0.66	-6%
Ultimate strength (MPa)	409	459	-10%